Gas-coupled laser acoustic detection as a non-contact line detector for photoacoustic and ultrasound imaging

2016 J. Opt. 18 024005

(http://iopscience.iop.org/2040-8986/18/2/024005)

IOP Publishing Journal of Optics
J. Opt. 18 (2016) 024005 (11pp) doi:10.1088/2040-8978/18/2/024005

Gas-coupled laser acoustic detection as a non-contact line detector for photoacoustic and ultrasound imaging

Jami L Johnson[1], Kasper van Wijk[1], James N Caron[2] and Miriam Timmerman[3]

[1] The Dodd-Walls Centre for Photonic and Quantum Technologies, Department of Physics, University of Auckland, Private Bag 92019, Auckland, New Zealand
[2] Research Support Instruments, 4325-B Forbes Boulevard, Lanham, MD 20706, USA
[3] Department of Biomechanical Engineering, University of Twente, Postbus 217, 7500 AE Enschede, The Netherlands

E-mail: jami.johnson@auckland.ac.nz

Received 21 August 2015, revised 7 December 2015
Accepted for publication 9 December 2015
Published 6 January 2016

Abstract

Conventional contacting transducers for ultrasonic wave detection are highly sensitive and tuned for real-time imaging with fixed array geometries. However, optical detection provides an alternative to contacting transducers when a small sensor footprint, a large frequency bandwidth, or non-contacting detection is required. Typical optical detection relies on a Doppler-shifted reflection of light from the target, but gas coupled-laser acoustic detection (GCLAD) provides an alternative optical detection method for photoacoustic (PA) and ultrasound imaging that does not involve surface reflectivity. Instead, GCLAD is a line-detector that measures the deflection of an optical beam propagating parallel to the sample, as the refractive index of the air near the sample is affected by particle displacement on the sample surface. We describe the underlying principles of GCLAD and derive a formula for quantifying the surface displacement from a remote GCLAD measurement. We discuss a design for removing the location-dependent displacement bias along the probe beam and a method for measuring the attenuation coefficient of the surrounding air. GCLAD results are used to quantify the surface displacement in a laser-ultrasound experiment, which shows 94% agreement to line-integrated data from a commercial laser vibrometer point detector. Finally, we demonstrate the feasibility of PA imaging of an artery-sized absorber using a detector 5.8 cm from a phantom surface.

Keywords: photoacoustic imaging, laser-ultrasound, beam deflection, gas-coupled laser acoustic detection, ultrasonics

(Some figures may appear in colour only in the online journal)

1. Introduction

Photoacoustic (PA) and laser-ultrasound (LU) modalities utilizing optical detection have the potential to substantially improve non-invasive medical imaging capabilities. However, hardware design toward a clinically feasible modality is not without challenges. Important considerations for detection of laser-induced acoustic waves include frequency bandwidth, detection aperture, and element size (Beard 2011). When a PA or LU wave travels through a sample, its surface is displaced. Traditional ultrasound transducers detect this movement using piezoelectric or ceramic crystals, while optical 'point' methods measure the change in optical path length with a probe beam perpendicular to the surface motion. Here, we present gas-coupled laser acoustic detection (GCLAD) (Caron *et al* 1998) for detecting PA and LU waves through air. GCLAD was developed for materials evaluation, and images of composite materials using a C-scan geometry have

been shown (Caron *et al* 2000). Here, we explore the possibility of GCLAD as an integrating line detector for PA and LU imaging.

Employing traditional ultrasound transducers for PA imaging is attractive, as it allows PA capabilities to be incorporated with commercially available ultrasound modalities. However, several characteristics of transducers are undesirable for PA imaging. Delivery of the source light in reflection mode is complicated with transducers, as most are contacting, relatively large and opaque devices that require an acoustic coupling medium. Photoacoustic waves are inherently broadband, thus the narrow frequency bandwidth of piezoelectric elements limits the size and depth of structures that can be imaged with a given transducer. Furthermore, the sensitivity of transducers decreases with element size. The assumption of a point detector required by most reconstruction algorithms is thus poorly satisfied, resulting in degraded images (Paltauf *et al* 2007).

Optical detection of ultrasound addresses many of the challenges associated with transducers. Examples include optical interferometers (Speirs and Bishop 2013), fiber Bragg detectors (Rosenthal *et al* 2011), micro-ring resonators (Ling *et al* 2011), and Fabry–Pérot sensors (Zhang *et al* 2008). These detectors have the benefit of broadband sensitivity and a point-like detection spot, therefore, spatial resolution is high compared to piezoelectric transducers. However, interferometric detection on scattering or absorbing surfaces, such as skin, often requires a reflective medium to be incorporated (Johnson *et al* 2014). Rousseau *et al* (2012a, 2012b) have shown adequate sensitivity with a fully non-contacting confocal Fabry–Pérot interferometer by employing a high-energy, pulsed probe beam. Likewise, Hochreiner *et al* (2012) used a two-wave mixing interferometer without the need for a coupling medium. However, interferometric detectors are difficult to parallelize, thus a single point is scanned across the sample surface for two- and three-dimensional imaging.

Integrating line detectors are a promising alternative to point detectors for PA imaging. While 2D imaging with point detectors of finite size is degraded by out-of-plane effects, waveforms acquired by line detectors strictly obey the two-dimensional wave equation when the line is much larger than the target (Paltauf *et al* 2007). Additionally, line detectors suppress signals with a wavelength such that destructive interference takes place along the line. In exploration geophysics, geophone groups are commonly used to suppress surface waves (often termed 'ground-roll') at the benefit of body-wave reflections from the targets of interest, by making the group-size equal to the wavelength of the surface-wave energy (section 4.4.2 of Kearey *et al* 2002). Analogously, line detection can suppress surface waves that interfere with the longitudinal waves of interest in medical LU imaging. The feasibility of Mach–Zehnder and Fabry–Pérot line detection in water has been shown (Grün *et al* 2009), and three-dimensional PA images of phantoms and insects were demonstrated using a Fabry–Pérot line detector (Grün *et al* 2010).

In this work, we present GCLAD as a quantitative integrating line detector. GCLAD is based on the deflection of an optical beam by ultrasound (Born and Wolf 1999), where the change in refractive index due to a propagating ultrasound wave is probed by a laser. This approach uses simple optics relative to interferometric techniques and requires minimal alignment. GCLAD is independent of surface reflectivity, and is therefore purely non-contacting and does not contribute to energy exposure. This is optimum for imaging when access to the target is required, or contact with the sample could cause discomfort or harm. Parallelization is straight-forward, and hardware is inexpensive, hence detector arrays for simultaneous acquisition of full-field data is possible.

Recently, the effects of gold nanoparticle concentration on PA waveforms have been monitored using beam deflection (Khosroshahi and Mandelis 2015). Further, PA waveforms have been detected with beam deflection in water, where Barnes *et al* (2014) demonstrated the ability to obtain directionality information, and Khachatryan *et al* (2014) designed a PA microscopy device using a C-scan approach. However, detection through air requires enhanced sensitivity, and the potential for line detection has not been studied until now.

In section 2, we derive the theory of GCLAD; section 3 presents a series of characterization experiments, demonstrating the feasibility of using GCLAD as a quantitative detector for PA and LU imaging; in section 4, we present a two-dimensional PA imaging experiment with GCLAD; and in section 5, we provide our discussion and conclusions. Throughout this work, all automation and data acquisition is controlled using PLACE, a Python-based open-source software package developed for experimental automation (Johnson *et al* 2015).

2. Gas-coupled laser acoustic detection

Laser-generated ultrasound is based on the conversion of a pulse of laser light to a pressure wave via thermoelastic expansion. This generation is described as PA when light is absorbed by molecules *inside* of a sample, and the conversion takes place at depth (Beard 2011, Blum *et al* 2011). Conversely, when the light is absorbed at the sample surface, generating elastic waves superficially, we call this technique LU (Scruby and Drain 1990). In general, the goal of medical PA imaging is to map optical properties of tissue, while LU is sensitive to the elastic properties alone.

The surface displacement resulting from a PA or LU wave propagating to the surface of a sample causes density variations in the surrounding air as the transmitted wave couples to the air. GCLAD detects these pressure variations by measuring the motion of an optical beam perpendicular to the acoustic propagation with a position-sensitive detector (PSD, Quarktet, Silver Springs, Maryland, USA). Theoretically, this approach has comparable sensitivity to ideal interferometers that require high surface reflectivity, but GCLAD is independent of surface optical properties (Caron 2008).

2.1. Relationship between refractive index and pressure in air

Here we derive a relationship between spatial and temporal variations in air pressure (caused by particle displacement in a sample), and the refractive index of air n. The Lorentz–Lorenz formula describes the relationship between the refractive index and the molar refractivity A of a substance (Born and Wolf 1999):

$$\frac{n^2 - 1}{n^2 + 2} = \frac{A\rho}{M}, \tag{1}$$

where ρ is density, and M is molecular mass. The refractive index of a gas can be found by taking the first-order Taylor expansion of equation (1) at $n = 1$:

$$\frac{2}{3}(n - 1) \approx \frac{A\rho}{M}, \tag{2}$$

and the ambient constants for refractive index n_0 and density ρ_0 can be related

$$\frac{(n_0 - 1)}{\rho_0} \approx \frac{3A}{2M}. \tag{3}$$

The density ρ of acoustic waves varies adiabatically with pressure p, thus

$$\frac{\partial p}{\partial \rho} = c^2, \tag{4}$$

and we can integrate to solve for the density of air for a given pressure

$$\rho = \frac{p - p_0}{c^2} + \rho_0. \tag{5}$$

Substituting equation (5) into equation (2) and defining the pressure of an acoustic wave $p(\mathbf{r}, t)$, we have a formula relating refractive index to pressure:

$$n(\mathbf{r}, t) \approx \frac{(n_0 - 1)(p(\mathbf{r}, t) - p_0)}{\rho_0 c^2} + n_0. \tag{6}$$

2.2. Ray theory of beam deflection

When an optical beam encounters a medium with a continuously varying refractive index, the beam is refracted according to the ray equation (Kopeika 1998):

$$\frac{\mathrm{d}}{\mathrm{d}s}\left(n\frac{\mathrm{d}\mathbf{r}}{\mathrm{d}s}\right) = \nabla n, \tag{7}$$

where n is the refractive index, s is the path length of the light ray, and $\mathbf{r}$ is the location of the ray in space (figure 1). For light propagating along an x-axis, $\mathrm{d}s \simeq \mathrm{d}x$ and equation (7) becomes the paraxial ray equation

$$\frac{\mathrm{d}}{\mathrm{d}x}\left(n\frac{\mathrm{d}\mathbf{r}}{\mathrm{d}x}\right) = \frac{\mathrm{d}n}{\mathrm{d}x}\frac{\mathrm{d}\mathbf{r}}{\mathrm{d}x} + n\frac{\mathrm{d}^2\mathbf{r}}{\mathrm{d}x^2} = \nabla n. \tag{8}$$

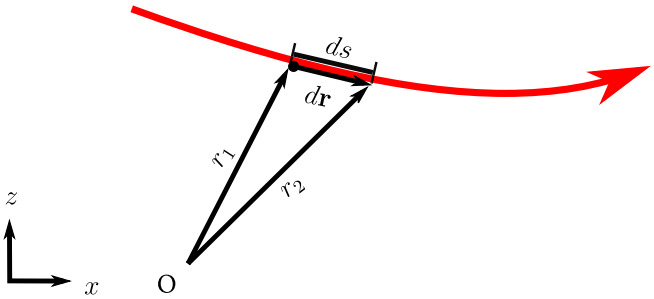

Figure 1. Geometry for ray propagation in an inhomogeneous medium.

Combining equation (6) and equation (8) for an acoustic plane wave propagating in the z-direction (figure 2) gives us

$$\left(\frac{(n_0 - 1)(p(z, t) - p_0)}{\rho_0 c^2} + n_0\right)\frac{\mathrm{d}^2 z}{\mathrm{d}x^2} = \frac{(n_0 - 1)}{\rho_0 c^2}\frac{\partial}{\partial z}p(z, t). \tag{9}$$

The index of refraction of air is close to unity, thus $n_0 - 1$ is small and $n_0 \gg \frac{(n_0 - 1)(p(z,t) - p_0)}{\rho_0 c^2}$. This simplifies equation (9) to

$$\frac{\mathrm{d}^2 z}{\mathrm{d}x^2} = \frac{(n_0 - 1)}{n_0 \rho_0 c^2}\frac{\partial}{\partial z}p(z, t). \tag{10}$$

Integrating with respect to x twice, we obtain

$$z(x) = ax^2 + bx + c, \tag{11}$$

where

$$a = \frac{(n_0 - 1)}{2n_0 \rho_0 c^2}\frac{\partial}{\partial z}p(z, t). \tag{12}$$

Assuming the light beam is incident parallel to the wavefront of the acoustic wave

$$b = \left.\frac{\mathrm{d}z}{\mathrm{d}x}\right|_{x=0} = \theta_0 = 0, \tag{13}$$

$$c = z|_{x=0} = 0, \tag{14}$$

and we have an equation for the displacement of a single optical ray propagating perpendicular to an acoustic plane wave

$$z(x) = \frac{(n_0 - 1)}{2n_0 \rho_0 c^2}\frac{\partial}{\partial z}p(z, t)x^2. \tag{15}$$

Equation (15) is valid across the length of interaction between the probe beam and the acoustic wave, x_s. Upon exiting the wave, the optical beam has been displaced through a total distance $z_s = z(x_s)$, corresponding to an angle $\theta \approx \tan(\theta) = \frac{z_s}{x_s}$, and

$$\theta \approx \frac{(n_0 - 1)}{2n_0 \rho_0 c^2}\frac{\partial}{\partial z}p(z, t)x_s. \tag{16}$$

The deflected wave continues to propagate unperturbed at an an angle θ with respect to the x axis where the total vertical

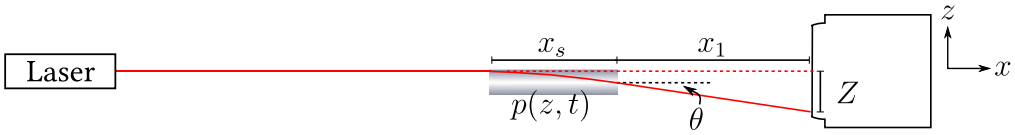

Figure 2. Measurement of an acoustic plane wave through air with gas-coupled laser acoustic detection. The continuously varying refractive index results in a position change in the z-direction, corresponding to an angle θ. The wave continues to propagate unperturbed, and is detected by a position-sensitive detector at a distance x_1.

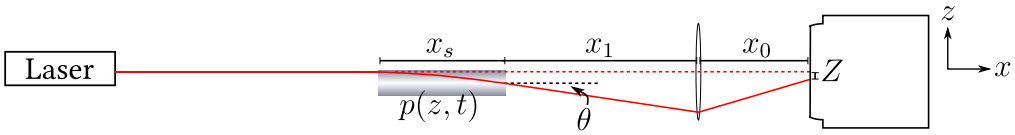

Figure 3. Gas-coupled laser acoustic detection with a convex lens placed in front of the position-sensitive detector. The dependence of Z on x_1 is removed when x_0 is equal to the focal length of the lens, creating a uniform response along the probe beam.

displacement is

$$Z = (x_s + x_1)\theta. \tag{17}$$

2.3. Dependence on acoustic source position

In a traditional beam deflection setup (figure 2), the total position change Z is proportional to the distance from the acoustic wave to the detector equation (17). As such, beam deflection is greater for a unit perturbation farther from the PSD than for one close to the PSD. To rectify this bias, a convex lens is placed in front of the position sensitive detector, as in figure 3. The position change at the PSD after passing through the lens can be determined from ray transfer (ABCD) matrix analysis. The contribution from a deflected ray is (Caron 2008):

$$z_\theta = x_0\theta + (x_1 + x_s)\left(1 - \frac{x_0}{f}\right)\theta, \tag{18}$$

and a displaced ray (traveling parallel to the original ray path) is

$$z_\parallel = \Delta z\left(1 - \frac{x_0}{f}\right), \tag{19}$$

where f is the focal length of the lens. When $x_0 \approx f$, the displacement term is negligible, and the deflected term is both directly proportional to θ and independent of x_1

$$Z = z_\theta + z_\parallel \approx x_0\theta. \tag{20}$$

Placing a lens at $x_0 \approx f$ is advantageous for line detection, as the amplitude is proportional to the change in pressure, but independent of the location of the acoustic waves along the probe beam. Furthermore, the sensitivity of the system can be tuned by varying the focal length of the lens (and changing x_0 accordingly), with the trade-off between sensitivity and compactness.

2.4. Quantifying surface displacement from beam deflection

Quantitative measurements of the displacement at the sample surface are possible given the beam deflection measured remotely. Upon reaching the surface of a sample, a propagating acoustic wave will displace the surface by a distance δ. Considering a planar surface, the wave will continue to propagate as a plane wave in the air defined (Towne 1967):

$$p(z, t) = k\rho_0 c^2 \delta \sin(kz - \omega t)\mathrm{e}^{-\alpha z}, \tag{21}$$

where ν is the frequency of the wave, $\omega = 2\pi\nu$, k is the wavenumber $\frac{\omega}{c}$, α is the attenuation coefficient, and z is the distance from the surface.

Substituting equations (16) and (21) into equation (20), we have an equation relating the total position change at the detector to the surface displacement of the sample:

$$Z = \frac{x_0 x_s}{2}\frac{(n_0 - 1)}{n_0}\delta\mathrm{e}^{-\alpha z}(k^2\cos(kz - \omega t) - \alpha k \sin(kz - \omega t)). \tag{22}$$

3. Characterization experiments

3.1. GCLAD as an unbiased line detector

Next, we compare GCLAD as an integrating line detector between a conventional beam deflection setup, and the unbiased approach described in section 2.3. First, we measure the GCLAD signal for an acoustic source at multiple positions along the probe beam using beam deflection as in figure 2. A 500 kHz transducer (V101, Panametrics, Olympus) driven by a 300 V square wave (5077PR, Olympus) with a 100 Hz repetition rate is used to generate acoustic waves. The transducer is mounted on a linear stage (M-IMS300LM, Newport, Irvine, CA, USA) 6 cm from the probe beam and scanned at 1 mm increments parallel to the detection line. The amplitude of the detected acoustic wave is recorded at each increment. In this configuration, the maximum amplitude is directly proportional to x_1 (figure 4). Second, we place a convex lens with a 60 mm focal length in front of the PSD where $x_0 \approx f$ and repeat the scan. As predicted by equation (20), the amplitude becomes uniform across the length of x_1.

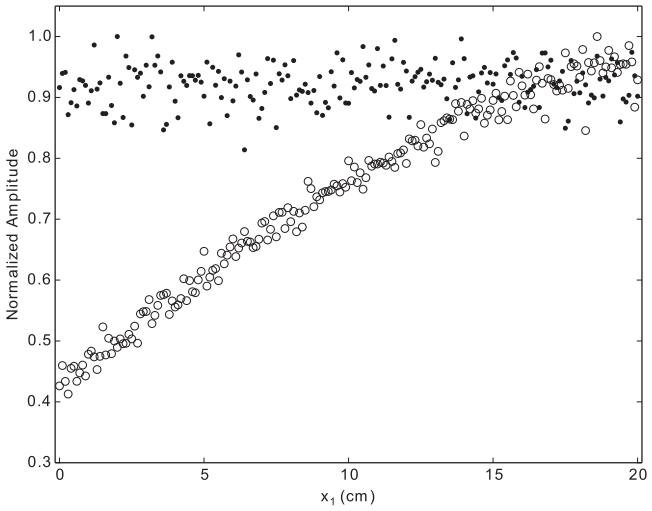

Figure 4. Maximum amplitude of an acoustic wave generated by a 500 kHz transducer and detected by GCLAD at discrete locations along the probe beam. With no lens in the setup, the amplitude increases with x_1 (∘). Incorporating a convex lens with a 60 mm focal length so that $x_0 \approx f$, the response is uniform for all x_1 (•).

3.2. Signal strength and laser fluence proportionality

For any quantitative acoustic detector, the amplitude of the detected wave must be proportional to the initial pressure distribution. To validate this property for GCLAD, we generate LU waves using four discrete light fluences and detect the elastic waves with GCLAD. A 3.3 cm thick solid phantom is composed of 1% Intralipid (Fresenius-Kabi, Uppsala, Sweden), 1% agar gel (A0930-05, US Biological, Swampscott, MA, USA), and 0.35% India ink, corresponding to an absorption coefficient of $\approx 20\,\mathrm{cm}^{-1}$ (Cubeddu *et al* 1997). The phantom is placed 9 mm from a GCLAD beam with a beam waist of 800 μm before the lens. A collimated 1064 nm source laser (Quanta-Ray INDI, Spectra-Physics, Newport, Irvine, CA, USA) with an 8 mm diameter is incident on the opposite side of the phantom (figure 5(a)). Laser-ultrasound waves are generated with laser fluences in the range of 70–100 mJ cm^{-2} in 10 mJ cm^{-2} increments at 10 Hz, and 64 waveforms were averaged for each fluence. As expected, figure 5(b) demonstrates that the signal amplitude is directly proportional to the incident laser fluence, and therefore the initial pressure of the LU wave.

3.3. Air gap dependence

A comprehensive understanding of the waveforms acquired by GCLAD after propagation through air is important for accurate analysis and reconstruction. Measuring relevant properties, such as velocity and attenuation, allows these parameters to be included in a reconstruction model.

To study the effects of the air gap for laser-generated ultrasound modalities, LU waves are generated with a 1064 cm Nd:YAG laser on a 1.5 cm thick solid tissue phantom composed of 1% Intralipid and 1% agar (figure 6(a)). An opaque tape with an unknown absorption coefficient is placed on the phantom surface to generate a localized LU wave at the phantom surface. The source laser is collimated with an 8 mm diameter and pulse energy of $\approx 150\,\mathrm{mJ\,cm}^{-2}$. This fluence is beyond the maximum permissible exposure for biological tissue (American National Standard for Safe Use of Lasers 2007); however, the energy is absorbed by the tape, rather than the tissue sample in this example. The wavefield propagates through the phantom, and is detected with GCLAD on the opposite side of the sample. An average of 200 waveforms is acquired every 1 mm up to 10 cm away from the phantom (figure 6(b)).

A slope correction obtained via linear regression corrects for the additional time travel through air and determines the velocity in air (344.3 m s^{-1}). With only the time-travel correction, the correlation coefficient for the direct wave is 0.91. The remaining difference is attributed to attenuation. The wavefield can be approximated by a plane wave when it crosses the phantom surface and geometric spreading is therefore minimal. The maximum amplitude decreases exponentially with an attenuation coefficient of 0.6 dB cm^{-1} (figure 6(c)), consistent with standard attenuation models

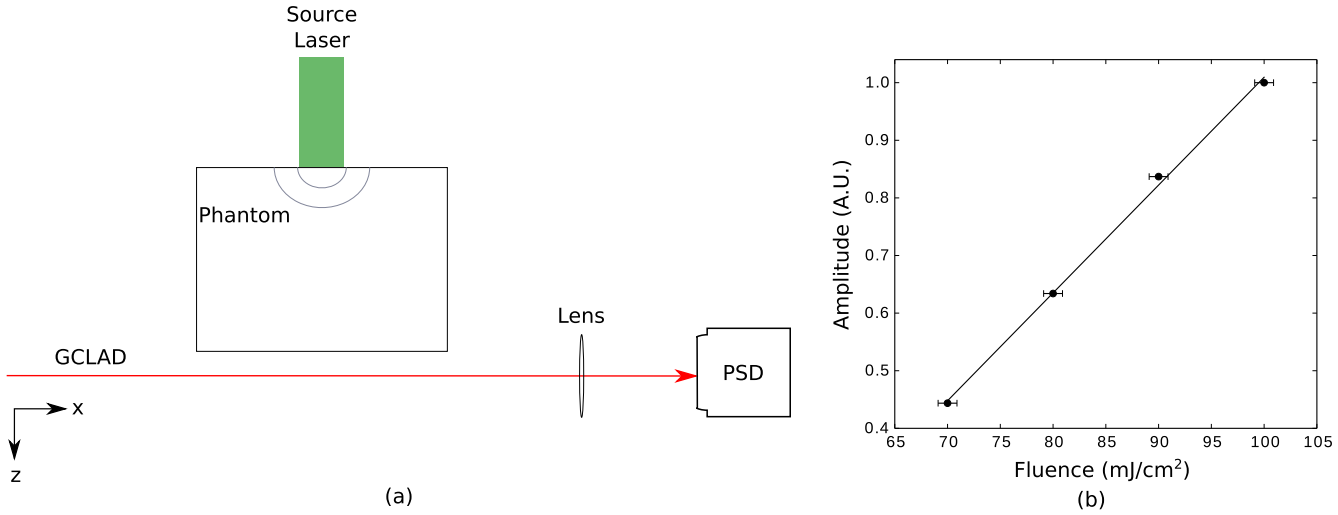

Figure 5. (a) Setup for measuring laser-ultrasound waves with GCLAD. (b) The amplitude of the laser-ultrasound waves increases proportional to the laser fluence. The error bars represent the standard error for the energy meter readings.

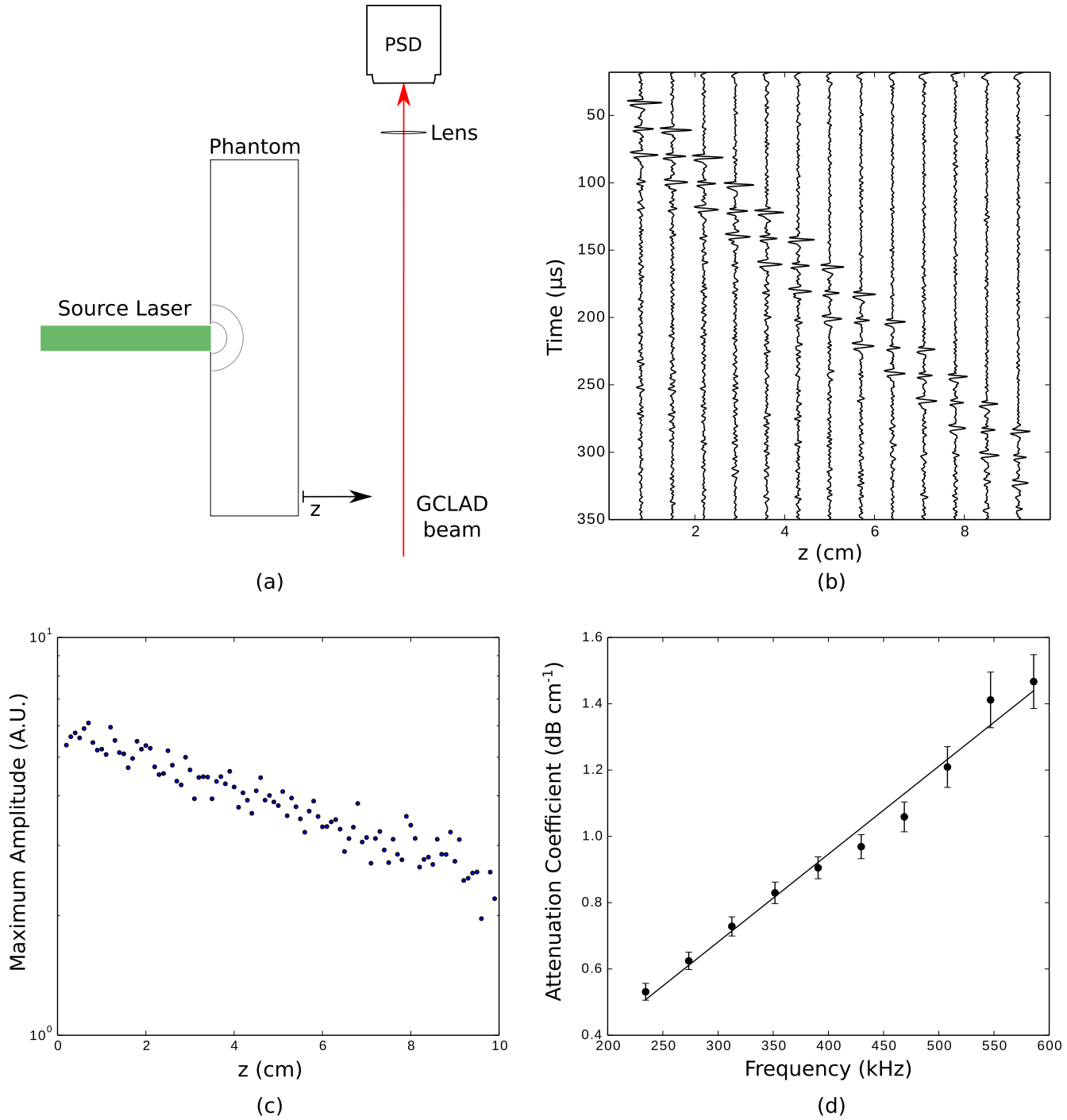

Figure 6. (a) Setup for air gap experiment. A laser-ultrasound wave is generated at the surface of a tissue phantom and detected with GCLAD up to 10 cm away from the phantom. (b) Acquired waveforms arriving at increasing delays, proportional to the distance from the phantom. The second and third arrivals in each waveform are reflections within the phantom. A subset of traces are shown for clarity. (c) The maximum amplitude of the direct wave attenuates exponentially. (d) The attenuation coefficient increases linearly with frequency. The error bars are the standard error of the linear regression used to find the relationship between power (dB) and each distance to the sample (z) for a given frequency.

(Hickling and Marin 1986). The frequency dependence of the attenuation coefficient is found by first plotting the power spectrum in decibels versus frequency for the signals recorded at each z-position. For each discrete frequency, the relationship between power and z-position is found to be linear. The slope of each of these frequency lines is plotted versus frequency to obtain figure 6(d), which shows a frequency-dependent attenuation coefficient (slope) of 2.7 dB cm^{-1} Hz^{-1}.

After the direct LU arrival, several reflections within the phantom are detected. The amplitude of each subsequent wave is decreased, with the exception of a slight increase in

amplitude of the third arrival compared to the second. With each pass through the phantom, the LU wave becomes more planar. The increase in amplitude seen in the third arrival indicates that it is more planar than the waves detected prior, thus the integrated signal along the GCLAD beam is higher. This highlights that amplitude quantification is dependent on the assumption of a plane wave, which is most accurate for waves travelling long distances.

These results confirm that higher frequencies are attenuated more strongly, therefore imaging small structures with high frequency content requires a small air gap, while larger structures with low dominant frequencies can be imaged farther from the sample. As the acoustic properties of air vary with environmental conditions, a reference air scan can be acquired at the time of data acquisition to calibrate the velocity and attenuation model.

3.4. Comparison to a commercial vibrometer

To compare GCLAD to state-of-the-art optical techniques and validate the amplitude quantification presented in section 2.4, we compare GCLAD to a commercial laser-Doppler vibrometer (OFV-505, Polytec, Irvine, CA, USA). The vibrometer records the particle displacement at a focused point in the direction perpendicular to the phantom surface using heterodyne-interferometry. We compare the average of a line of these point measurements to a single waveform recorded by GCLAD.

A solid phantom is composed of 1% Intralipid, 1% agar gel, and 0.35% India ink. The GCLAD beam is directed in the x-direction—parallel to the phantom surface—with an air gap of 9 mm (figure 7(a)). The vibrometer sensor head is mounted on a high-resolution linear stage (M-IMS300LM), with the probe beam directed perpendicular to the phantom surface (z) in the same plane as the GCLAD beam. To enhance reflectivity for detection with the vibrometer, a retroreflective tape is placed across the phantom surface.

A LU wave is generated on the surface of the phantom with a 1064 nm Nd:YAG laser with a pulse energy of 100 mJ cm^{-2}, collimated 8 mm beam diameter, and 10 Hz repetition rate. A single GCLAD waveform is recorded as the average of 64 realizations. Next, the vibrometer scans across 4 cm of the surface in the x-direction in increments of 250 μm, as denoted by the dotted line in figure 7. The average of 64 waveforms detected by the vibrometer is recorded at each point.

The relationship between the GCLAD signal amplitude and beam deflection (Z) is determined with a calibration scan (figure 7(c)). The GCLAD probe laser is fixed to a mirror mount with nanometer-precision motors (8310, NewFocus, Newport, Irvine, CA, USA) replacing the fine-adjustment screws on two perpendicular axes. The laser mount is rotated through an angle of 720 μrad in the z-direction. At increments of 3.6 μrad, the DC signal detected with the position-sensitive detector is recorded. The paraxial approximation is applied, and a linear relationship between deflection and signal amplitude was found with a slope of 110 mV μm^{-1}.

To quantify the surface displacement from the measured beam deflection, we apply equation (22) using values $n_0 = 1.000\,2919$ (Born and Wolf 1999), $\alpha = 0.6$ dB cm^{-1} (section 3.3), $c = 345$m s^{-1}, $x_s = 4.5$ cm, and the maximum frequency in the Fourier spectrum of the LU wave is $\nu \approx$ 850 kHz. The waveforms detected by the vibrometer from all positions are averaged and compared with the calibrated GCLAD waveform. The direct waves have a correlation coefficient of 0.94 for the time window shown in figure 7(b). The discrepancy is largely due to the curvature remaining in the LU wave before coupling to the air.

4. Two-dimensional imaging with GCLAD

Finally, we perform a two-dimensional PA imaging experiment with GCLAD. A 5.6 mm diameter polyester tube with a 25.4 μm wall (Vention Medical 103-0481, Salem, NH, USA) is embedded 1.2 cm deep in a solid tissue phantom (1% Intralipid, 1% agar). The tube is filled with infrared absorbing dye (Epolight 2057, Epolin, Newark, NJ, USA) with an absorption coefficient of approximately 10 cm^{-1}, according to the manufacturer-specified absorptivity. A collimated 1064 nm source laser is aligned with the GCLAD beam, creating a transmission-mode experiment (figure 8). The source laser has a 100 mJ cm^{-2} fluence, 8 mm beam diameter, and 10 Hz repetition rate. The phantom is placed 5.8 cm from the GCLAD beam on a high-resolution linear stage (M-IMS300LM). A B-Scan is recorded across 85 mm of the phantom surface by moving the phantom in 250 μm steps in the x-direction, with an average of 64 GCLAD waveforms recorded at each increment.

The acquired wavefields after removal of the travel time through air are shown in figure 9(a). The source energy is attenuated as it propagates through the phantom, therefore the strongest absorption occurs at the interface of the dye and tube wall closest to the source surface, while absorption is weaker at the tube wall closest to the GCLAD surface. This non-uniform light distribution, combined with the strong acoustic contrast between the tube wall and the dye, results in a dual-arrival of PA waves from a single tube. The PA wave generated by the tube wall closest to the detector arrives first (1), and the PA wave generated at the wall closest to the source arrives later, but with a higher amplitude (2). These waves are diffracted at the corner of the phantom and travel along the detection surface (3). Photoacoustic waves also propagate to the source surface where they are reflected and propagate back to the detection surface (4, 5).

The waves arriving after the direct PA waves (1, 2) are muted, and we use time reversal (Shragge *et al* 2015, Johnson *et al* 2015) to reconstruct the location of the tube, as shown in figure 8(b). The generation of dual PA waves results in an image that highlights the top and bottom edges of the tube, a known effect when large, uniform PA sources are used (Gateau *et al* 2013).

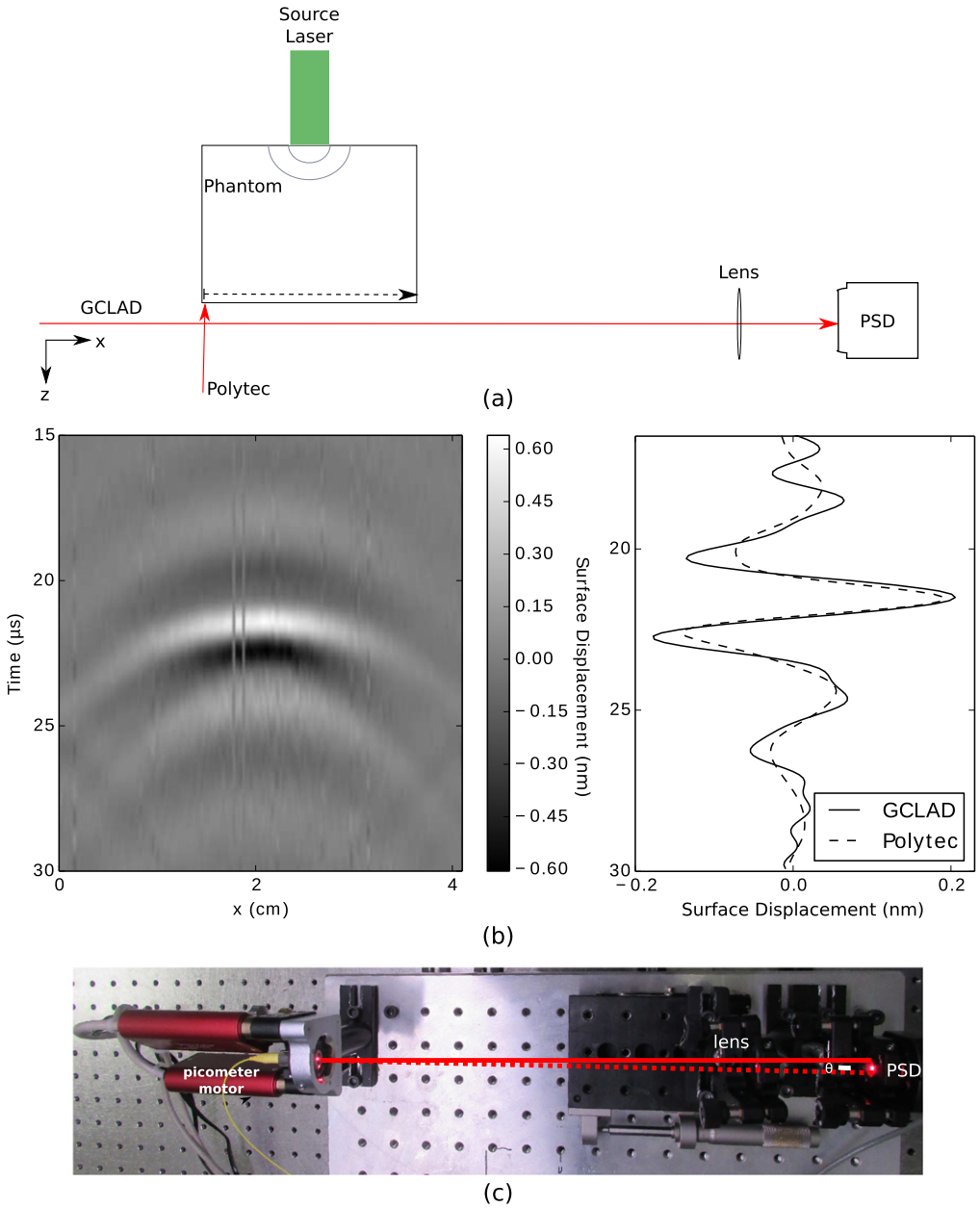

Figure 7. (a) Setup for detecting laser-ultrasound waves with line and point measurements. The GCLAD probe beam is parallel to the phantom surface and a single waveform is acquired. A commercial vibrometer (Polytec) is directed perpendicular to the surface and scanned in the x-direction denoted by the dotted line. (b) Polytec waveforms measured at each point along the phantom surface are shown on the left. The LU wave exhibits some curvature upon reaching the surface, before coupling to the air. The right-hand side shows the quantified GCLAD waveform compared to the average of the Polytec measurements. (c) Setup for calibration scan. A picomotor controlled mirror displaces the beam an angle θ, and the corresponding voltage from the position-sensitive detector (PSD) is recorded.

5. Discussion

We have demonstrated the feasibility of gas-coupled laser acoustic detection as a non-contact line detector for PA and LU imaging. In section 2, we derived a formula for quantifying the displacement of a sample surface from a GCLAD signal detected in the surrounding air equation (22). This formula assumes a uniform response along the probe beam, and requires knowledge of the distance the beam is deflected at the PSD and the attenuation and speed of sound in the air. In section 2.3, a lens is placed one focal length from the PSD, which results in an unbiased response along the probe beam. This response is shown to be proportional to the initial pressure distribution in section 3.2. The attenuation coefficient and speed of sound in air is measured in section 3.3. In section 3.4, equation (22) is applied to quantify the surface displacement of a tissue phantom due to an incident LU wave. This quantification utilizes the properties of air found in section 3.3 as well as a calibration scan relating the signal amplitude to deflection angle. The quantified GCLAD waveform is compared to the average of a line of point measurements acquired with a commercial laser-Doppler

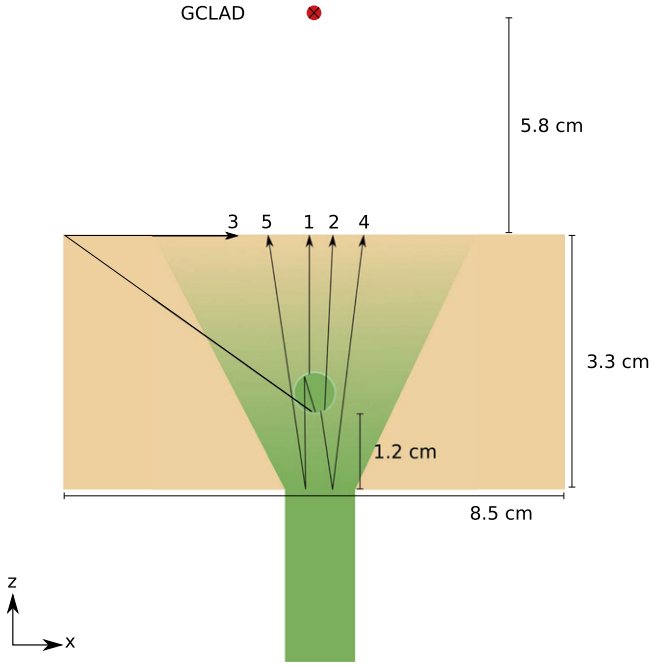

Figure 8. Setup for acquisition of two-dimensional PA wavefields with GCLAD. A 5.6 mm diameter tube (25.4 μm wall) is embedded 1.2 cm from the source surface. The source laser and GCLAD are configured in transmission mode, with GCLAD directed out of the page. The phantom is translated in the x-direction. The arrows correspond to raypaths of PA waves generated at the tail of the arrow.

vibrometer. Our results show excellent agreement and demonstrate that quantitative measurements of surface displacement can be found given the beam deflection measured remotely by utilizing simple calibration scans of a GCLAD system. Finally, in section 4, we present a phantom experiment that demonstrates the feasibility of imaging objects of comparable size to major blood vessels using GCLAD detection 5.8 cm from the sample surface. The direct PA waves and reflections and diffractions within the phantom are detected, and we reconstruct the PA image using time reversal.

Finally, we would like to address the limitations of the assumptions made in section 2, as well as the frequency bandwidth and sensitivity of GCLAD. Due to the small velocity of sound in air compared to tissue, even a small distance between the sample surface and probe beam corresponds to a relatively large travel time delay (1mm equates to roughly 3 μs of travel time). Therefore, a measure of surface topography may be required for accurate reconstruction when the acquisition surface is not flat. This can be accomplished using a complementing modality, such as optical coherence tomography, to measure the surface topography (Rousseau *et al* 2012b) and a reconstruction algorithm that accounts for these variations (Shragge 2014). Additionally, a primary assumption of this work is that a plane wave is incident on the sample surface and propagates as a plane wave through the air perpendicular to the GCLAD beam. PA waves are directional, and may be incident obliquely on the sample surface. Upon transmitting from the sample to the air, the acoustic waves will slow significantly and flatten due to the rapid decrease in velocity, however, some curvature may remain (section 3.3). Furthermore, the sensitivity of GCLAD decreases with $\sin^2(\theta)$, where θ is the angle between the optical beam and the direction of ultrasound propagation (Caron 1997, Caron and Kunapareddy 2014). The largest contribution to the signal amplitude is waves propagating normal to the surface.

The sensitivity of GCLAD is affected by several sources of noise. Light interference on the highly sensitive position-sensitive detector can significantly affect the signal-to-noise; therefore, the position-sensitive detector should ideally be housed in a light-proof enclosure. Theoretically, GCLAD has comparable sensitivity to an ideal reflectivity-dependent confocal Fabry–Pérot interferometer, particularly in the 1–3 MHz range (Caron 2008). However, GCLAD's sensitivity is ultimately limited by the sensitivity of the photodetector and the noise and beam quality of the probe laser. In section 3.4, we measured surface displacements smaller than 0.2 nm with a signal-to-noise of 13.5 dB.

The frequency bandwidth of this air-coupled technique is limited by both the width of the probe beam and the

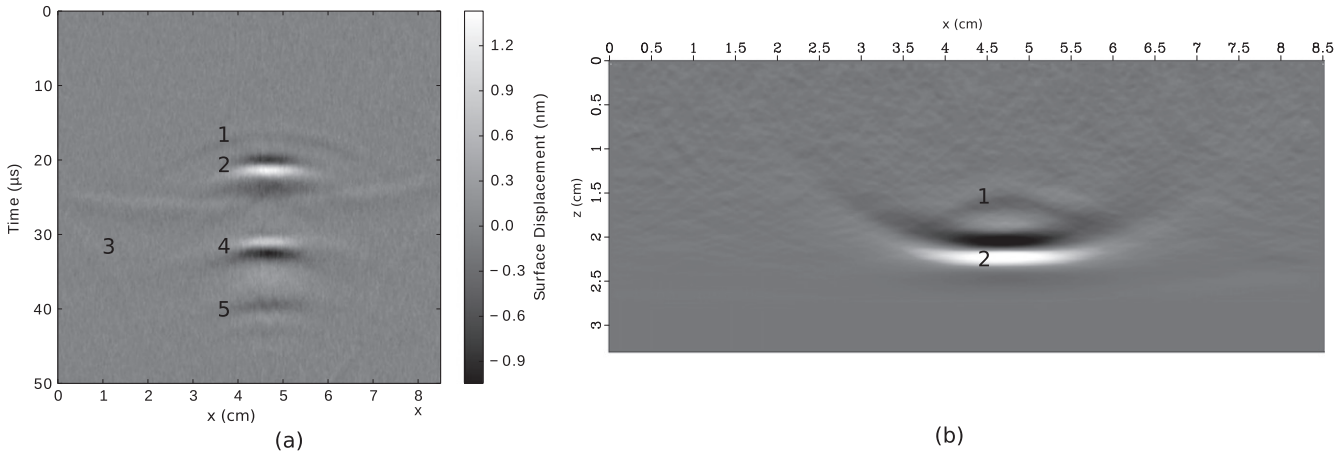

Figure 9. Two-dimensional (a) PA wavefields and (b) PA image reconstructed with time reversal. The numbers correspond to waves generated in the tube and at the phantom surface that follow the raypaths labeled in figure 8 and are described in the text.

attenuation coefficient in air. The theory described in section 2 assumes the probe beam is a single ray. In reality, the probe beam has a finite width, thus the temporal resolution (and therefore reconstructed pressure distribution) broadens proportional to the beam width. In both sections 3.3 and 3.4, the highest frequency detected is ~0.85 MHz. This is slightly higher than the expected frequency limit with an 800 μm probe beam diameter, and likely due to the Gaussian profile of the probe beam. The beam can be collimated to a smaller diameter to improve the temporal resolution, or focused to a point near the imaged object. However, resolution broadens away from the focus (Paltauf *et al* 2009).

In conclusion, this work demonstrates the first application of GCLAD as a non-contact line detector for medical imaging. The signal amplitude of GCLAD is independent of the surface reflectivity of the sample, thus no coupling or reflective layer is needed. This opens up applications where contact with the sample is harmful or inconvenient, and simplifies delivery of the source light when a reflection configuration is required. We have derived and experimentally validated a method for quantifying the displacement at a sample surface from a GCLAD measurement, and shown that this technique is on par with commercial optical detectors that rely on a reflective surface. In addition to characterizing and quantifying several properties of GCLAD, we presented an experiment where a 5.6 mm diameter phantom vessel was imaged using a detector 5.8 cm from the surface. Future work will build on these results, and include additional geometries for two- and three-dimensional imaging.

References

American National Standards Institute 2007 ANSI Z136.1 American National Standard for Safe Use of Lasers (Laser Institute of America, Orlando, FL)

Barnes R A, Maswadi S, Glickman R and Shadaram M 2014 Probe beam deflection technique as acoustic emission directionality sensor with photoacoustic emission source *Appl. Opt.* **53** 511–9

Beard P 2011 Biomedical photoacoustic imaging *Int. Focus* **1** 602–31

Blum T E, van Wijk K, Snieder R and Willis M E 2011 Laser excitation of a fracture source for elastic waves *Phys. Rev. Lett.* **107** 275501

Born M and Wolf E 1999 *Principles of Optics* 7th edn (New York: Cambridge University Press)

Caron J and Kunapareddy P 2014 Atypical applications for gas-coupled laser acoustic detection *J. Phys.: Conf. Ser.* **520** 012022

Caron J N 1997 Application of laser ultrasonics to graphite/polymer composites *PhD Thesis* University of Delaware

Caron J N 2008 Displacement and deflection sensitivity of gas-coupled laser acoustic detection *1st Int. Symp. on Laser Ultrasonics: Science, Technology and Applications*

Caron J N, Steiner K V, Yuqiao Y and Mehl J B 2000 Gas coupled laser acoustic detection for ultrasound inspection of composite materials *Mater. Eval.* **58** 667–71

Caron J N, Yang Y, Mehl J B and Steiner K V 1998 Gas-coupled laser acoustic detection at ultrasonic and audio frequencies *Rev. Sci. Instrum.* **69** 2912–7

Cubeddu R, Pifferi A, Taroni P, Torricelli A and Valentini G 1997 A solid tissue phantom for photon migration studies *Phys. Med. Biol.* **42** 1971–9

Gateau J, Chaigne T, Katz O, Gigan S and Bossy E 2013 Improving visibility in photoacoustic imaging using dynamic speckle illumination *Opt. Lett.* **38** 5188–91

Grün H, Berer T, Burgholzer P, Nuster R and Paltauf G 2010 Three-dimensional photoacoustic imaging using fiber-based line detectors *J. Biomed. Opt.* **15** 021306

Grün H, Berer T, Hochreiner A, Nuster R, Paltauf G and Burgholzer P 2009 Photoacoustic imaging with integrating line detectors *SPIE Medical Imaging* (International Society for Optics and Photonics) p 72650K

Hickling R and Marin S P 1986 The use of ultrasonics for gauging and proximity sensing in air *J. Acoust. Soc. Am.* **79** 1151–60

Hochreiner A, Berer T, Grün H, Leitner M and Burgholzer P 2012 Photoacoustic imaging using an adaptive interferometer with a photorefractive crystal *J. Biophotonics* **5** 508–17

Johnson J L, Shragge J and van Wijk K 2015 Image reconstruction of multi-channel photoacoustic and laser-ultrasound data using reverse time migration *SPIE BiOS* (International Society for Optics and Photonics) p 932314

Johnson J L, tom Wörden H and van Wijk K 2015 PLACE: an open-source Python package for laboratory automation, control, and experimentation *J. Lab. Autom.* **20** 10–6

Johnson J L, van Wijk K and Sabick M 2014 Characterizing phantom arteries with multi-channel laser ultrasonics and photo-acoustics *Ultrasound Med. Biol.* **40** 513–20

Kearey P, Brooks M and Hill I 2002 *An Introduction to Geophysical Exploration* 3rd edn (Malden: Blackwell Science Ltd)

Khachatryan E, Maswadi S, Tsyboulski D, Barnes E, Oraevsky A, Nash K and Glickman R 2014 Optoacoustic microscopy using laser beam deflection technique *SPIE BiOS* (International Society for Optics and Photonics) p 89432T

Khosroshahi M E and Mandelis A 2015 Combined photoacoustic ultrasound and beam deflection signal monitoring of gold nanoparticle agglomerate concentrations in tissue phantoms using a pulsed Nd: YAG laser *Int. J. Thermophys.* **36** 880–90

Kopeika N S 1998 *A System Engineering Approach to Imaging* (Bellingham: SPIE Press)

Ling T, Chen S-L and Guo L J 2011 Fabrication and characterization of high Q polymer micro-ring resonator and its application as a sensitive ultrasonic detector *Opt. Express* **19** 861–9

Paltauf G, Nuster R and Burgholzer P 2009 Characterization of integrating ultrasound detectors for photoacoustic tomography *J. Appl. Phys.* **105** 102026

Paltauf G, Nuster R, Haltmeier M and Burgholzer P 2007 Experimental evaluation of reconstruction algorithms for limited view photoacoustic tomography with line detectors *Inverse Problems* **23** S81–94

Rosenthal A, Razansky D and Ntziachristos V 2011 High-sensitivity compact ultrasonic detector based on a pi-phase-shifted fiber bragg grating *Opt. Lett.* **36** 1833–5

Rousseau G, Blouin A and Monchalin J-P 2012a Non-contact photoacoustic tomography and ultrasonography for tissue imaging *Biomed. Opt. Express* **3** 16–25

Rousseau G, Gauthier B, Blouin A and Monchalin J-P 2012b Non-contact biomedical photoacoustic and ultrasound imaging *J. Biomed. Opt.* **17** 061217

Scruby C B and Drain L E 1990 *Laser Ultrasonics Techniques and Applications* (Bristol: Adam Hilger)

Shragge J 2014 Reverse time migration from topography *Geophysics* **79** S141–52

Shragge J, Blum T E, van Wijk K and Adam L 2015 Full-wavefield modeling and reverse time migration of laser ultrasound data: a feasibility study *Geophysics* **80** D553–63

Speirs R W and Bishop A I 2013 Photoacoustic tomography using a Michelson interferometer with quadrature phase detection *Appl. Phys. Lett.* **103** 053501

Towne D H 1967 *Wave Phenomena* (Reading, MA: Addison-Wesley)

Zhang E, Laufer J and Beard P 2008 Backward-mode multiwavelength photoacoustic scanner using a planar Fabry–Perot polymer film ultrasound sensor for high-resolution three-dimensional imaging of biological tissues *Appl. Opt.* **47** 561–77